

High-Bandwidth Sensorless Algorithm for AC Machines Based on Square-Wave-Type Voltage Injection

Young-Doo Yoon, *Member, IEEE*, Seung-Ki Sul, *Fellow, IEEE*, Shinya Morimoto, and Kozo Ide, *Member, IEEE*

Abstract—This paper describes a new control algorithm which can enhance the dynamics of a sensorless control system and gives a precise sensorless control performance. Instead of the conventional sinusoidal-type voltage injection, a square-wave-type voltage injection incorporated with the associated signal processing method is proposed in this paper. As a result, the error signal can be calculated without low-pass filters and time delays, and the position estimation performance can be enhanced. Using the proposed method, the performance of the sensorless control can be enhanced; the bandwidth of the current controller was enhanced up to 250 Hz, and that of the speed controller was up to 50 Hz.

Index Terms—AC machines, induction machine, sensorless control, signal injection, square-wave voltage, synchronous machine.

I. INTRODUCTION

SENSORLESS drives of ac motors are adopted in many applications from industrial applications to home appliances. Recently, electric vehicle applications have also been reported [1]–[3]. The advantages of sensorless drives are not only the reduction in the cost and size but also the improvement of the reliability by eliminating the position sensor and related cable connections. To achieve the advantages, many sensorless techniques for estimating rotor position and speed have been reported. These techniques are classified into two categories: techniques based on back electromotive force (EMF) [4]–[7] and techniques based on saliency in the spatial impedance of the motor [8]–[16].

The former uses voltage models [4], [5] and/or observers [6], [7] in the synchronous or stationary reference d - q frame. It presents good results in the middle- and high-speed regions. Since the amplitude of back EMF is proportional to the rotor speed, it cannot keep the performance in the low-speed region,

including zero speed and/or frequency, where the back EMF disappears. The latter are exploiting the magnetic saliency. Some algorithms inject test voltage signals in a sampling period to estimate the rotor position [8], [9]. Since they detect inductance difference using voltage signals in a short time, they can be frail to parameter variation or measurement noises. Other algorithms inject rotating high-frequency voltages and use a tracking algorithm [10], [11]. The other algorithms inject pulsating high-frequency voltages [12]–[16]. These rotating and pulsating high-frequency voltage injection methods were proposed for zero and/or low-frequency operation. These methods can be applied to general ac machines. They give reasonable torque control capability at zero and/or low frequency, even under heavily loaded conditions.

Based on such progresses, sensorless algorithms are adopted in general-purpose inverters to drive interior permanent magnet (IPM) motors. However, the performance of the conventional sensorless control methods is still insufficient for some applications. The bandwidth of a speed controller is limited up to a few hertz. Therefore, in some areas, a position sensor is used in normal operations due to the limitation of the performance of the sensorless control, and sensorless algorithms are just utilized as the backup system for emergency when the position sensor fails.

In this paper, a new algorithm of sensorless control for ac servo applications is proposed to enhance the performance of sensorless drive. Considering zero- and low-speed operations, this paper focuses on voltage injection methods. Moreover, the method based on back-EMF voltage is not considered. However, the proposed method can be combined with the method based on back-EMF voltage in middle- and high-speed operations just like other previous methods [1], [16].

When high-frequency injection methods with conventional manners (sinusoidal voltage injection) are used, low-pass filters (LPFs) should be used to get an error signal. However, these LPFs degrade sensorless control performances because of the inherent time delay of LPFs. To enhance the performance, the delay should be minimized. The proposed method relies on higher frequency square-wave-type voltage injection. As a result, the error signal can be calculated without any LPF, and that means no time delay. Hence, the position estimation performance can be enhanced. As a consequence, bandwidths of current, speed, and position controllers can be increased very much compared to those by the conventional sinusoidal-type voltage injection method.

Manuscript received June 7, 2010; revised November 9, 2010; accepted December 15, 2010. Date of publication March 14, 2011; date of current version May 18, 2011. Paper 2010-IDC-229.R1, presented at the 2009 IEEE Energy Conversion Congress and Exposition, San Jose, CA September 20–24, and approved for publication in the IEEE TRANSACTIONS ON INDUSTRY APPLICATIONS by the Industrial Drives Committee of the IEEE Industry Applications Society.

Y.-D. Yoon is with Samsung Electronics, Suwon 443-742, Korea (e-mail: youngdoo.yoon@gmail.com).

S.-K. Sul is with Seoul National University, Seoul 151-741, Korea (e-mail: sulsk@plaza.snu.ac.kr).

S. Morimoto and K. Ide are with Yaskawa Electric Company, Kitakyushu 803-8530, Japan (e-mail: sinyam@yaskawa.co.jp; kozo@yaskawa.co.jp).

Color versions of one or more of the figures in this paper are available online at <http://ieeexplore.ieee.org>.

Digital Object Identifier 10.1109/TIA.2011.2126552

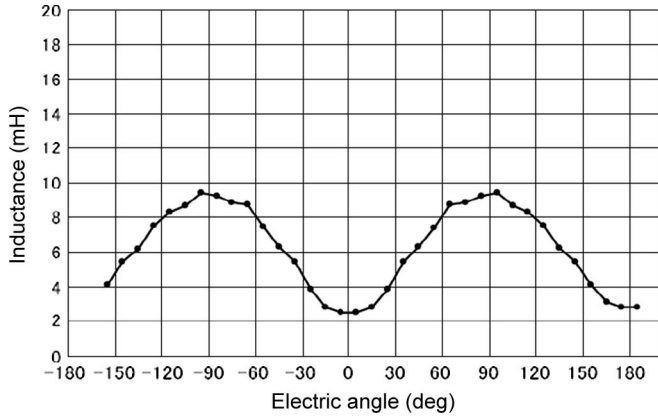


Fig. 1. Inductance characteristics of the tested motor.

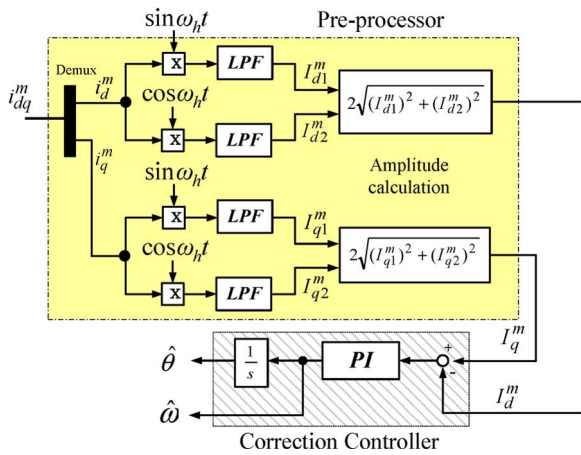


Fig. 2. Block diagram of a signal processing and a position observer.

II. ANALYSIS OF CONVENTIONAL SENSORLESS ALGORITHM

Conventional sensorless algorithms [10]–[16] based on a high-frequency injection method exploit the saliency of the motor at the injected high frequency. Fig. 1 shows the high-frequency inductance characteristics of an IPM motor. Using this saliency with a high-frequency injection method, sensorless algorithms extract the angle information. Then, a position observer estimates the rotor position. Fig. 2 shows a typical block diagram of signal processing methods, including a correction controller to estimate the rotor position. From the diagram, it can be seen that the sensorless algorithm consists of a high-frequency voltage injection part, a signal processing part, and a correction controller which is basically a kind of position observer. In this section, a conventional voltage injection method and a signal processing method are explained, respectively.

A. Analysis of Voltage Injection Method

In Fig. 3, the block diagram of a conventional high-frequency voltage injection method [10]–[16] is shown. High-frequency voltage at the rotor reference d - q frame is added to the output of the current controller. Although, in the block diagram, the high-frequency voltage is injected in the rotor reference frame,

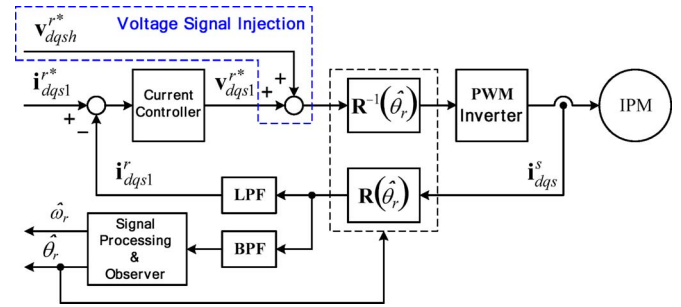


Fig. 3. Block diagram of voltage injection method.

the voltage can be injected in the stationary reference frame, too. In both cases, the motor current consists of a fundamental component and the injected high-frequency component. The fundamental component of the motor current is extracted through an LPF or a notch filter, and it is used as a feedback to the current controller to regulate the torque and flux level of the motor. The high-frequency component of the motor current is extracted using a bandpass filter, and it is used as input to a signal processing part including a position observer.

There are roughly two kinds of voltage injection methods. One is a rotating voltage injection method in the stationary reference frame [10], [11]. The other is a pulsating voltage injection method in the d -axis of the estimated rotor reference frame [12]–[16].

Basic information of every signal processing method is the induced high-frequency current in the stationary reference frame i_{dqsh}^s which is the only measurable quantity [12]. Therefore, i_{dqsh}^s should be analyzed according to voltage injection methods. Here, a pulsating voltage injection method in the d -axis of the estimated rotor reference frame will be analyzed. In this paper, notation “ h ” means the injected high-frequency component.

When a pulsating voltage is injected into the d -axis of the estimated rotor reference frame, injected high-frequency voltage can be described as in (1) with the assumption that the estimation error of the rotor position ($\tilde{\theta}_r = \theta_r - \hat{\theta}_r$) is small enough

$$v_{ds}^{\hat{r}} = V_h \cos \omega_h t, \quad v_{qs}^{\hat{r}} = 0, \quad \tilde{\theta}_r = \theta_r - \hat{\theta}_r \approx 0. \quad (1)$$

The relationship between the induced high-frequency current and voltage can be described as follows:

$$\begin{bmatrix} v_{dsh}^r \\ v_{qsh}^r \end{bmatrix} = [Z^r] \begin{bmatrix} i_{dsh}^r \\ i_{qsh}^r \end{bmatrix} = [Z^r] [R(\theta_r)] \begin{bmatrix} i_{dsh}^s \\ i_{qsh}^s \end{bmatrix}. \quad (2)$$

Therefore, the induced high-frequency current can be deduced as follows:

$$\begin{aligned} \begin{bmatrix} i_{dsh}^s \\ i_{qsh}^s \end{bmatrix} &= [R(\theta_r)]^{-1} [Z^r]^{-1} \begin{bmatrix} v_{dsh}^r \\ v_{qsh}^r \end{bmatrix} \\ &= [R(\theta_r)]^{-1} [Z^r]^{-1} [R(\tilde{\theta}_r)] \begin{bmatrix} v_{dsh}^{\hat{r}} \\ v_{qsh}^{\hat{r}} \end{bmatrix}. \end{aligned} \quad (3)$$

$\omega_h L_{dh}^r$ and $\omega_h L_{qh}^r$ are generally much larger than R_{dh}^r and R_{qh}^r in the high-frequency impedance model. Moreover, the

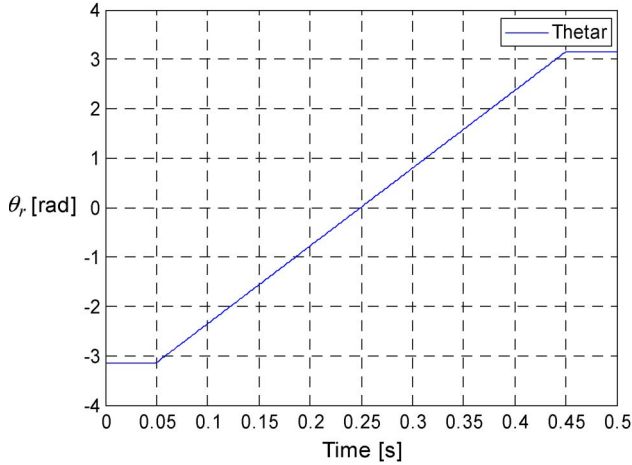


Fig. 4. Variation of the rotor angle to verify the characteristics of the induced high-frequency current.

injected frequency ω_h is also at least one order larger than the fundamental frequency ω_r . Therefore, the high-frequency impedance in the rotor reference frame Z^r can be simplified as follows:

$$\begin{aligned} [Z^r] &= \begin{bmatrix} R_{dh}^r + L_{dh}^r \cdot s & -\omega_r L_{qh}^r \\ \omega_r L_{dh}^r & R_{qh}^r + L_{qh}^r \cdot s \end{bmatrix} \\ &\approx \begin{bmatrix} L_{dh}^r \cdot s & 0 \\ 0 & L_{qh}^r \cdot s \end{bmatrix}. \end{aligned} \quad (4)$$

Using (3) and (4), the induced high-frequency current can be represented as follows. In (5), the last expression is described to intuitively understand the high-frequency current. High-frequency injection methods cannot be used when saliency does not appear

$$\begin{aligned} \begin{bmatrix} i_{dsh}^s \\ i_{qsh}^s \end{bmatrix} &\approx \frac{V_h \sin \omega_h t}{\omega_h} \begin{bmatrix} \frac{\cos(\theta_r) \cos(\tilde{\theta}_r)}{L_{dh}^r} + \frac{\sin(\theta_r) \sin(\tilde{\theta}_r)}{L_{qh}^r} \\ \frac{\sin(\theta_r) \cos(\tilde{\theta}_r)}{L_{dh}^r} - \frac{\cos(\theta_r) \sin(\tilde{\theta}_r)}{L_{qh}^r} \end{bmatrix} \\ &\approx \frac{V_h \sin \omega_h t}{\omega_h L_{dh}^r} \begin{bmatrix} \cos(\theta_r) \\ \sin(\theta_r) \end{bmatrix} \end{aligned} \quad (5)$$

(Under the assumption that $\tilde{\theta}_r \approx 0$).

When rotor position θ_r changes from $-\pi$ to π as shown in Fig. 4, the induced high-frequency current i_{dqsh}^s is shown in Fig. 5 which is the simulation results using the aforementioned sensorless control. Here, the envelope of the d -axis induced high-frequency current shows the cosine function of rotor position, and that of the q -axis induced high-frequency current shows the sine function of rotor position.

To demonstrate this definitely, the bold lines are also overlaid in Fig. 5 together with the d - and q -axis induced high-frequency currents. The bold line in the d -axis waveform shows $\cos(\theta_r)$, and that in the q -axis waveform shows $\sin(\theta_r)$. From this figure, it can be concluded that it is possible to detect the rotor position by tracking the envelope of the induced high-frequency current i_{dqsh}^s when a high-frequency voltage is injected into the d -axis

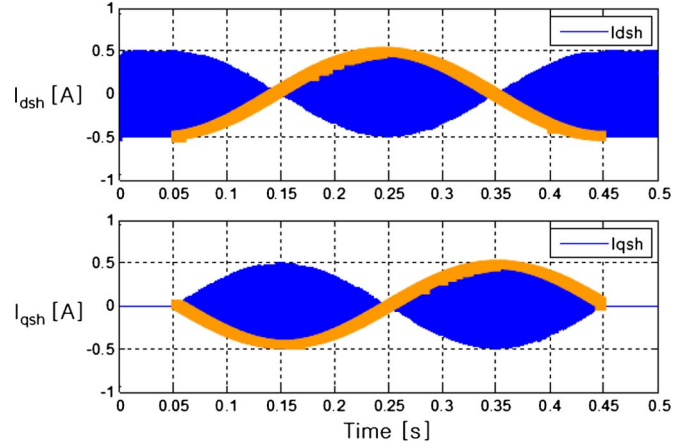


Fig. 5. Envelope of the induced high-frequency current.

of the estimated rotor reference frame under the assumption of small enough error between the actual rotor position and the estimated position.

Therefore, the rotor position can be extracted only by rejecting the injected frequency from the induced high-frequency current i_{dqsh}^s . Using arctangent function as (6), the rotor position can be directly calculated. In a real system, however, the real implementation of (6) is quite difficult or impossible since the denominator of (6) could be very small and/or zero in every cycle of the injected signal and the angle through (6) is quite sensitive to the measurement noises

$$\begin{aligned} \begin{bmatrix} \frac{i_{dsh}^s}{\sin \omega_h t} \\ \frac{i_{qsh}^s}{\sin \omega_h t} \end{bmatrix} &\approx \begin{bmatrix} \frac{1}{L_{dh}^r \omega_h} \cos(\theta_r) \\ \frac{1}{L_{dh}^r \omega_h} \sin(\theta_r) \end{bmatrix} \quad (\because \tilde{\theta}_r \approx 0), \\ \theta_{rCal} &= \text{atan2} \left(\frac{i_{qsh}^s}{\sin \omega_h t}, \frac{i_{dsh}^s}{\sin \omega_h t} \right). \end{aligned} \quad (6)$$

B. Signal Processing Method

When a pulsating voltage injection method in the d -axis of the estimated rotor reference frame is applied, two kinds of signal processing methods can be generally utilized. These methods can be classified by current measurement reference frames. One is the method using the measurement axis in [12] and [13] which uses the current at the reference frame offset by 45° from the estimated rotor reference frame. The other could be called as the “method using i_{qsh}^r ” in [14] and [15] which uses the q -axis current in the estimated rotor reference frame. Here, the method in [15] will be analyzed.

Fig. 6 shows the block diagram of the “method using i_{qsh}^r ”. As shown in Fig. 6, this method uses the q -axis induced high-frequency current in the estimated rotor reference frame. The main idea for this method is that the injected voltage at the d -axis in the real rotor reference frame should induce only d -axis current.

The high-frequency model of the plant can be described as

$$\begin{bmatrix} v_{dsh}^r \\ v_{qsh}^r \end{bmatrix} = \begin{bmatrix} R_{dh}^r + L_{dh}^r \cdot s & -\omega_r L_{qh}^r \\ \omega_r L_{dh}^r & R_{qh}^r + L_{qh}^r \cdot s \end{bmatrix} \begin{bmatrix} i_{dsh}^r \\ i_{qsh}^r \end{bmatrix}. \quad (7)$$

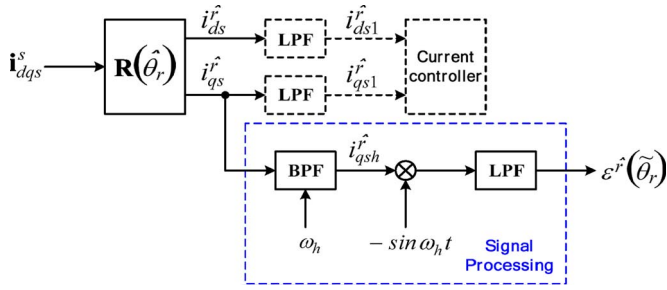


Fig. 6. Block diagram of “method using i_{qsh}^r ”

From (7), $-i_{qsh}^r \sin \omega_h t$ can be described as follows:

$$-i_{qsh}^r \sin \omega_h t = \frac{V_{inj}}{2} \left[\frac{\omega_r L_{diff}^r - 2\omega_r L_{avg}^r \cos 2\tilde{\theta}_r}{2\omega_h^2 L_{dh}^r L_{qh}^r} \sin 2\omega_h t + \frac{L_{diff}^r \sin 2\tilde{\theta}_r (1 + \cos 2\omega_h t)}{\omega_h L_{dh}^r L_{qh}^r} \right] \quad (8)$$

$$L_{avg}^r \equiv \frac{L_{dh}^r + L_{qh}^r}{2}, \quad L_{diff}^r \equiv L_{dh}^r - L_{qh}^r. \quad (9)$$

As shown in (8), the estimation error of rotor position $\tilde{\theta}_r \equiv \theta_r - \hat{\theta}_r$ is included in $-i_{qsh}^r \sin \omega_h t$. Error signals, including $\tilde{\theta}_r$, can be extracted by using an LPF. Equation (10) shows the result after ideal low-pass filtering

$$LPF(-i_{qsh}^r \sin \omega_h t) = \frac{V_{inj} L_{diff}^r}{4\omega_h L_{dh}^r L_{qh}^r} \sin 2\tilde{\theta}_r \equiv \varepsilon^r(\tilde{\theta}_r). \quad (10)$$

Though only one signal processing method has been addressed here, most of signal processing methods with high-frequency injection methods have something in common. They use LPFs to get error signals. This is because the injected frequency component should be rejected. However, an LPF results in a time delay in position and speed estimation, and this delay limits all the performance of sensorless control.

On the contrary, there are other sensorless approaches [8], [17], [18] such as the “INFORM” method and zero sequence technique. They do not use LPFs so that they have better performances than the conventional methods. However, they need additional circuits such as voltage sensors and/or custom-designed hardware. Standard pulsewidth modulation (PWM) controllers cannot be used.

C. Challenges to Increase Bandwidth of Sensorless Control

The conventional position observer—correction controller—may be a form of a proportional–integral (PI) controller or a form of a proportional–integral–derivative (PID) controller with torque feedforward. As mentioned in the previous section, signal processing methods incorporate an LPF to obtain an estimation error of the rotor position. Furthermore, the speed estimation, used as a feedback signal for the speed control loop, also needs an LPF since the estimated speed from the position observer is noisy. Therefore, the realistic implementation of a position observer is not a simple form of a PI or PID controller. Fig. 7 shows a possible

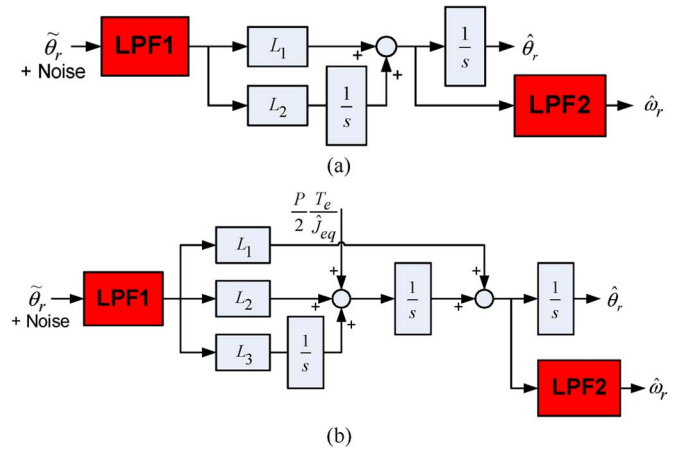


Fig. 7. Realistic forms of conventional position observer. (a) PI form. (b) PID form.

implementation of the position and speed observer. As shown in Fig. 7, LPF1 and LPF2 are included in the position observer loop.

These LPFs restrict the control bandwidth. At first, LPF1 is related with the bandwidth of the position observer. When the cutoff frequency of LPF1 is high, which means that LPF1 is weak, the input of the position observer has severe noise. Moreover, if LPF1 is strong, which means that the cutoff frequency of LPF1 is low, the position observer loop has severe time delay. Therefore, in both cases, the bandwidth of the position observer is restricted. Because of the noise sensitivity and the delay, it makes the observer unstable when the bandwidth is tempted to increase.

LPF2 is related with the bandwidth of the speed controller. When LPF2 is weak, the feedback of the speed controller has severe noise. Moreover, when LPF2 is strong, it makes severe delay in the speed controller loop. In both cases, the bandwidth of the speed controller is also restricted. Because of the noise sensitivity and the delay, it degrades the performance of the speed controller when the bandwidth is getting extended.

As mentioned before, LPFs restrict the bandwidth of the position observer and the speed controller. Therefore, in order to increase bandwidths, LPFs should be eliminated or be weak.

III. PROPOSED SENSORLESS ALGORITHM

As mentioned before, the envelopes (bold lines) of i_{dqsh}^s in Fig. 5 denote the rotor position. Therefore, the rotor position can be extracted only by rejecting the injected high frequency from the induced current i_{dqsh}^s . Using arctangent function as (6), the rotor position can be directly calculated. In this case, an LPF may not be used to get the rotor position, and there is no delay in rotor position estimation. In a real system, however, (6) is not possible to be implemented as described before.

In order to get a rotor position as (6) in a real system, the high-frequency sine function $\sin \omega_h t$ should be eliminated from i_{dqsh}^s . To that purpose, a method to inject square-wave-type voltage in the d -axis of the estimated rotor reference frame is

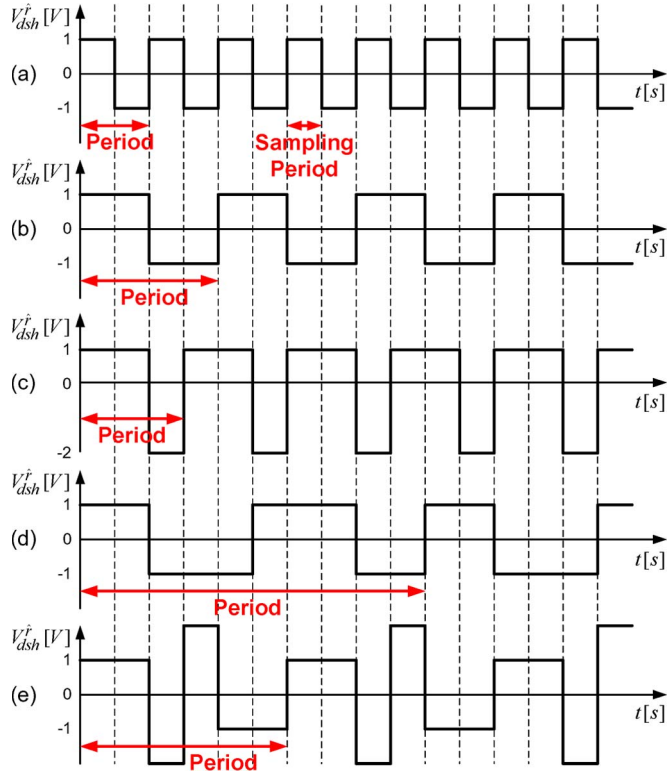


Fig. 8. Several possible square-wave-type injection voltages.

proposed in this paper. The injected voltage is described as

$$V_{dsh}^{\hat{r}} = \begin{cases} V_h, & \text{half duty} \\ -V_h, & \text{otherwise} \end{cases} \quad (V_h > 0), \quad V_{qsh}^{\hat{r}} = 0 \quad (11)$$

where V_h is the magnitude of injection voltage. The injected voltage can be several different square-wave-type voltages as shown in Fig. 8. However, for convenience of the explanation, the voltage described by (11), shown in Fig. 8(b), is used for the analysis.

To get better performances, the maximum injection frequency can be up to a half of the switching frequency. The reason is for the digital implementation of the notch filter, which is used for the feedback of the current controller. If the high-frequency induced current is not properly filtered out, the output voltage of the current regulator would interfere with the injection voltage because the filtered current is utilized for the feedback of the current regulator. Moreover, it would degrade the overall performance. Another reason is to minimize the noise in the induced current due to the sampling delay and/or the nonideal components in the signal processing. Furthermore, if the space vector PWM is used to apply voltage into the motor, the noise in the induced current would be minimized due to the symmetric voltage pulse pattern.

Fig. 9 shows the pattern of injection voltage under the conditions that the switching frequency is 10 kHz, the injection frequency is 5 kHz, and the magnitude of injection voltage is 8 V. These values depend on motor and inverter parameters and the desired performance.

When the square-wave-type voltage in Fig. 9 is injected, the corresponding Δi_{dqsh}^s can be described as (12) shown at the

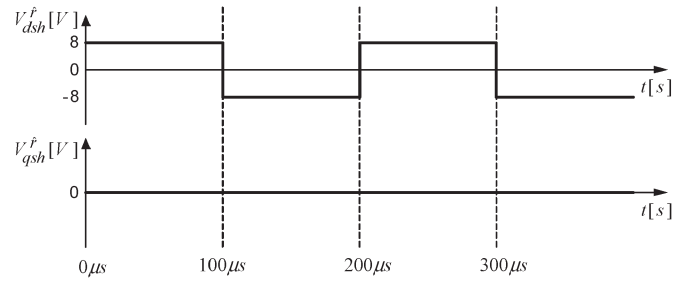


Fig. 9. Pattern of a square-wave-type injection voltage described by (11).

bottom of the page. Here, “ Δ ” means the difference between the present value and the previous value of sampling instants.

$$\begin{aligned} & \begin{bmatrix} \Delta i_{dsh}^s \\ \Delta i_{qsh}^s \end{bmatrix} \\ &= [R(\theta_r)]^{-1} [Z^r]^{-1} [R(\tilde{\theta}_r)] \begin{bmatrix} v_{dsh}^{\hat{r}} \\ v_{qsh}^{\hat{r}} \end{bmatrix} \\ &\approx \begin{cases} V_h \Delta T \cdot \begin{bmatrix} \frac{\cos(\theta_r) \cos(\tilde{\theta}_r)}{L_{dh}^r} + \frac{\sin(\theta_r) \sin(\tilde{\theta}_r)}{L_{qh}^r} \\ \frac{\sin(\theta_r) \cos(\tilde{\theta}_r)}{L_{dh}^r} - \frac{\cos(\theta_r) \sin(\tilde{\theta}_r)}{L_{qh}^r} \end{bmatrix}, & V_{dsh}^{\hat{r}} > 0 \\ -V_h \Delta T \cdot \begin{bmatrix} \frac{\cos(\theta_r) \cos(\tilde{\theta}_r)}{L_{dh}^r} + \frac{\sin(\theta_r) \sin(\tilde{\theta}_r)}{L_{qh}^r} \\ \frac{\sin(\theta_r) \cos(\tilde{\theta}_r)}{L_{dh}^r} - \frac{\cos(\theta_r) \sin(\tilde{\theta}_r)}{L_{qh}^r} \end{bmatrix}, & V_{dsh}^{\hat{r}} < 0 \end{cases} \end{aligned} \quad (12)$$

To consider the polarity of the injection voltage, (12) can be modified as

$$\begin{aligned} \Delta i_{dsh}^s ' &= \begin{cases} \Delta i_{dsh}^s, & \text{if } V_{dsh}^{\hat{r}} > 0 \\ -\Delta i_{dsh}^s, & \text{otherwise} \end{cases} \\ \Delta i_{qsh}^s ' &= \begin{cases} \Delta i_{qsh}^s, & \text{if } V_{dsh}^{\hat{r}} > 0 \\ -\Delta i_{qsh}^s, & \text{otherwise.} \end{cases} \end{aligned} \quad (13)$$

Finally, $\Delta i_{dqsh}^s '$ can be expressed as (14). The last expression in (14) is also described to intuitively understand the high-frequency current. The proposed method cannot be used when saliency does not appear

$$\begin{aligned} & \begin{bmatrix} \Delta i_{dsh}^s ' \\ \Delta i_{qsh}^s ' \end{bmatrix} = V_h \Delta T \cdot \begin{bmatrix} \frac{\cos(\theta_r) \cos(\tilde{\theta}_r)}{L_{dh}^r} + \frac{\sin(\theta_r) \sin(\tilde{\theta}_r)}{L_{qh}^r} \\ \frac{\sin(\theta_r) \cos(\tilde{\theta}_r)}{L_{dh}^r} - \frac{\cos(\theta_r) \sin(\tilde{\theta}_r)}{L_{qh}^r} \end{bmatrix} \\ &\approx \frac{V_h \Delta T}{L_{dh}^r} \cdot \begin{bmatrix} \cos(\theta_r) \\ \sin(\theta_r) \end{bmatrix} \\ & \quad (\text{Under assumption that } \tilde{\theta}_r \approx 0). \end{aligned} \quad (14)$$

Using $\Delta i_{dqsh}^s '$, the calculated rotor position θ_{rCal} can be directly calculated as (15). In (6), the denominator value of the two inputs of the atan2 function goes to zero in every cycle of the injected signal. At the instant, the result from the atan2 function is quite sensitive to the measurement noises. However, in (15), the two inputs of the atan2 function have bounded values so that the result from atan2 is robust to the noises.

Moreover, the error signal of the position observer $f(\tilde{\theta}_r)$ is directly calculated from θ_{rCal} as (16). Therefore, θ_{rCal} and

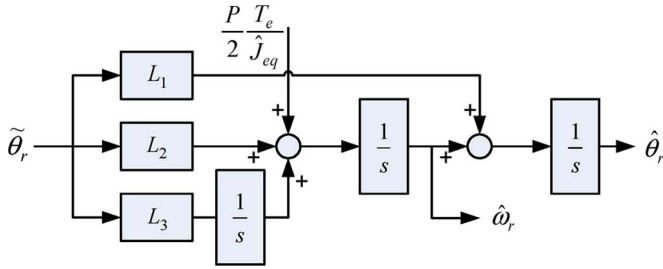


Fig. 10. Block diagram of the proposed position observer.

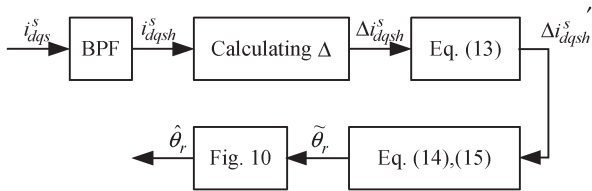


Fig. 11. Block diagram of the proposed demodulation method.

$f(\tilde{\theta}_r)$ can be obtained at every sampling instant without any LPF, and there is no time delay in the signal processing

$$\theta_{rCal} = \text{atan2}(\Delta i_{qsh}^{s'}, \Delta i_{dsh}^{s'}) \quad (15)$$

$$f_1(\tilde{\theta}_r) \equiv \theta_{rCal} - \hat{\theta}_r \approx K_{error1} \tilde{\theta}_r \quad (\tilde{\theta}_r \approx 0). \quad (16)$$

Using the proposed method, the error signal of the position observer $f(\tilde{\theta}_r)$ can be obtained without any LPF. Therefore, LPF1 shown in Fig. 7 can be eliminated. To further remove LPF2, the speed controller can be implemented based on another state of the position observer for a feedback. Fig. 10 shows a block diagram of the position observer exploiting the advantage of the proposed method. Fig. 11 shows the overall block diagram of the proposed demodulation method from the stator currents to the estimated rotor position $\hat{\theta}_r$.

Comparing Figs. 7 and 10, it can be seen that two LPFs have disappeared in Fig. 10. It means that the major cause to limit the dynamics of sensorless control is removed. Therefore, by using the proposed method, the bandwidth of the position observer and speed controller can be extended compared to that of the conventional method. The performance comparison between the conventional and the proposed signal processing method in conjunction with the new injection method and observer design can be summarized as follows.

- Two LPFs are removed.
 - There is virtually no delay in tracking the rotor position.
- Injection frequency becomes higher.
 - Fundamental and injection frequencies are definitely separated.
- Stability of overall system is improved.
 - Bandwidth of the position observer can be increased.
 - Bandwidth of the speed and position controller can be increased.

TABLE I
NOMINAL PARAMETERS OF MOTOR UNDER THE TEST

Quantity	Value [Unit]
Rated Power	80 [W]
Rated Torque	0.5 [Nm]
Rated Current	2.1 [A _{RMS}]
Rated Speed	1500 [r/min]
Dc Link Voltage	50 [V]
Stator Resistance	1.53[Ω]
Stator Inductance	$L_d = 3$ [mH], $L_q = 9$ [mH]
Overall Inertia	11.72e-5 [kg·m ²]

IV. EXPERIMENTAL RESULTS

The proposed method can be applied to any kind of ac machines which has saliency in the rotor impedance. Here, an IPM synchronous machine (IPMSM) was selected for the experiments to verify the effectiveness of the proposed method. The nominal parameters of a motor under the test are listed in Table I.

The switching frequency was set as 10 kHz, and the sampling frequency was 20 kHz. The square-wave high-frequency voltage was injected. In the cases of position control and speed control, the magnitude of the injection voltage was 8 V, and its frequency was 5 kHz. It was added to the output voltage of the current controller, and the sum was synthesized by a commercial inverter.

The bandwidths of the speed and position controller were set as 50 and 10 Hz, respectively. The pole of the position observer was set as 50 Hz, and the PI gains of the position observer were tuned. The bandwidth of the current controller was 250 Hz. The cutoff frequency of the notch filter for the feedback of the current controller was set as the injection frequency.

Fig. 12 shows the waveform of stator currents in the stationary reference d - q frame on a constant speed operation at 100 r/min. Due to the high-frequency injection, they have ripples. Fig. 12(b) shows the magnified waveform. The proposed method utilizes these high-frequency currents to estimate the rotor position.

Fig. 13 shows the position estimation performance on a constant speed operation at 100 r/min. $\Delta i_{dqsh}^{s'}$, the calculated position θ_{rCal} , the estimated position through the observer $\hat{\theta}_r$, and the real position by the attached encoder for monitoring purpose θ_r are displayed. As shown in Fig. 13, the calculated position θ_{rCal} had some noises, but the estimated position $\hat{\theta}_r$ had virtually no noise due to the position observer. From this figure, it can be concluded that the proposed method estimates the rotor position quite well without any time delay.

Fig. 14 shows the current regulation performance at the standstill. The d -axis current in the rotor reference frame was regulated with a sine wave reference. The magnitude of the current reference was 1 A, and the frequency was 250 Hz. In Fig. 14(a) and (b), the offsets of the current reference were 0 A and 1.5 A, respectively. IdseNF represents the d -axis current filtered by the notch filter. In Fig. 14(a), IdseNF was slightly distorted due to the zero-current clamping effect [19]. In Fig. 14(b), it can be seen that IdseNF was regulated well.

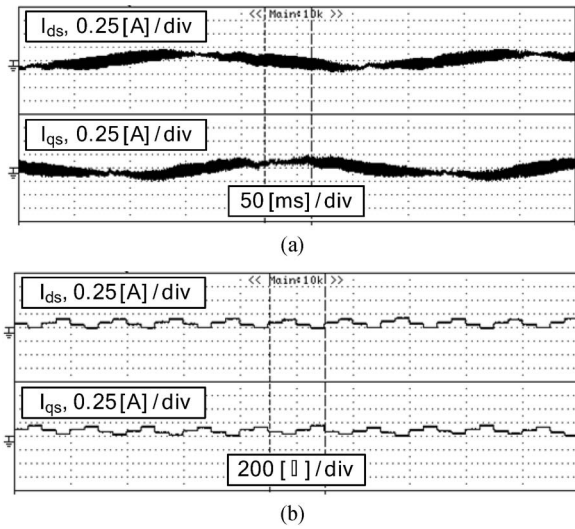


Fig. 12. Waveforms of the machine currents. (a) Stator currents in stationary reference $d-q$ frame. (b) Magnified waveform.

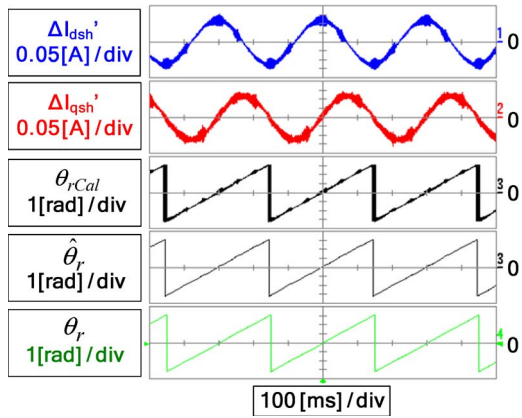


Fig. 13. Position estimation performance.

Experiments on a speed control mode were performed as shown in Figs. 15–17. Fig. 15 shows the step response when the output of the speed controller—torque reference—is not saturated. The step response with the reference changes from 300 to 400 r/min is shown. As shown in Fig. 15, the speed was well regulated, and the bandwidth can be figured out as 50 Hz, which is the designed value.

Fig. 16 shows the step response when the output of the speed controller is saturated. The step response with the reference changes from 0 to 1500 r/min is shown. As shown in Fig. 16, speed was increasing as a ramp since torque reference was limited.

Fig. 17 shows the sine wave response of the speed controller to show the bandwidth of the speed regulator clearly. The magnitude of the speed reference was set as 100 r/min, and the frequencies were set as 10 and 50 Hz, respectively. As shown in these figures, speed was well regulated up to the designed bandwidth, which was 50 Hz.

Moreover, the Bode plot was used for evaluating the performance of the current regulator and speed controller. Generally, the current regulation loop is considered as the first

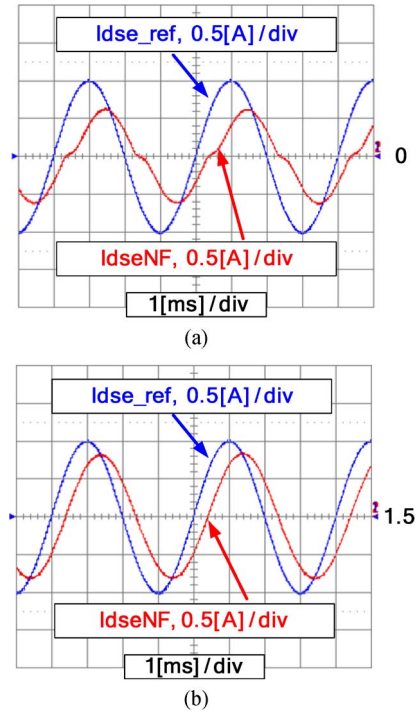


Fig. 14. Current regulation performance. (a) Offset of current command is 0 A. (b) Offset of current command is 1.5 A.

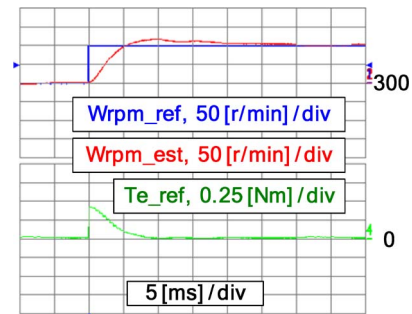


Fig. 15. Step response of speed controller when the output of the speed controller is not saturated.

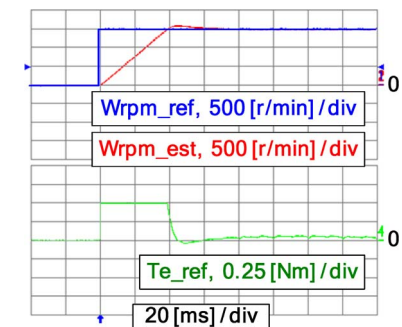


Fig. 16. Step response of speed controller when the output of the speed controller is saturated.

LPF ($i_{dqs}^r/i_{dqs}^{r*} = \omega_c/(s + \omega_c)$); therefore, the bandwidth of the regulator is defined as the frequency where 3 [dB] attenuation of the actual current compared to its reference in the Bode plot occurs. However, the exact transfer function of the loop including delays cannot be modeled as the first

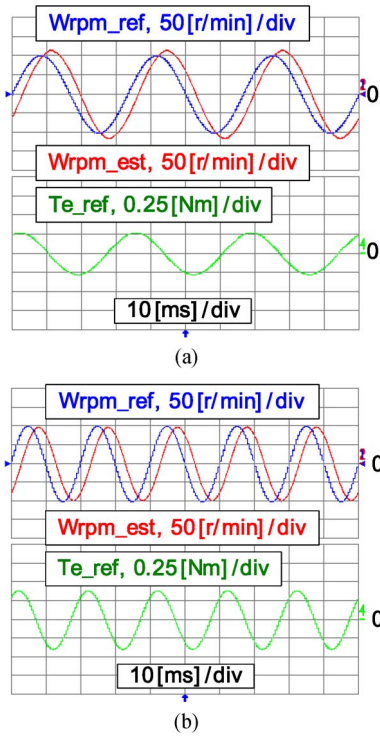


Fig. 17. Speed regulation performance. (a) 30-Hz operation. (b) 50-Hz operation.

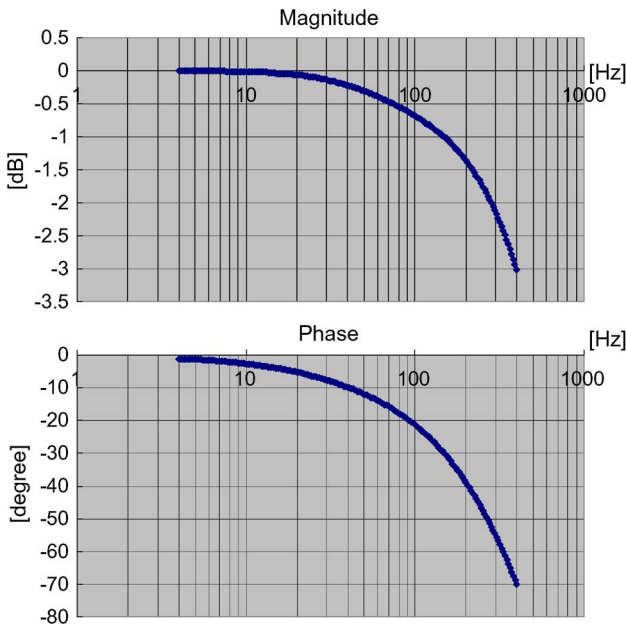


Fig. 18. Bode diagram of the current regulation.

LPF, and sometimes, the frequency in the Bode plot where 45 [deg] phase delay occurs may be considered as the bandwidth. Fig. 18 shows the Bode plot of the current feedback loop. The bandwidth of the current regulator is almost 250 Hz.

Fig. 19 shows the Bode plot of the speed feedback loop. If the frequency where 45 [deg] phase delay occurs is considered as the bandwidth of the regulator, the bandwidth of the speed regulator is almost 40 Hz. That is slightly less than the designed bandwidth.

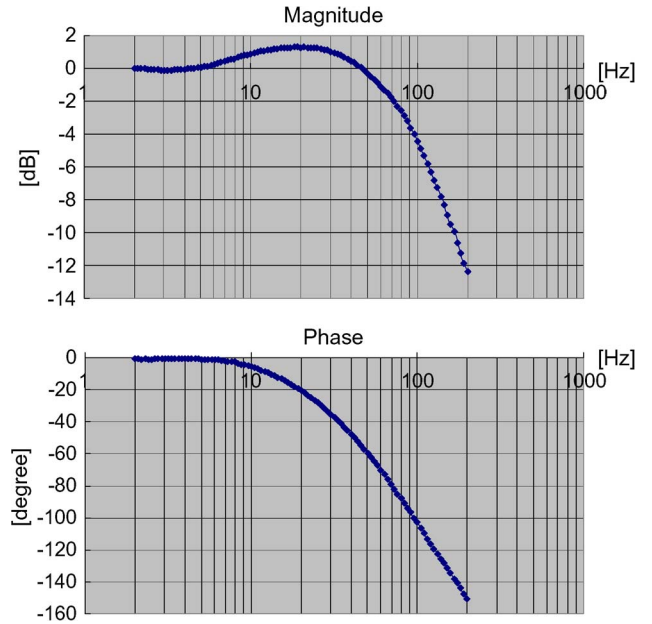


Fig. 19. Bode diagram of the speed regulation.

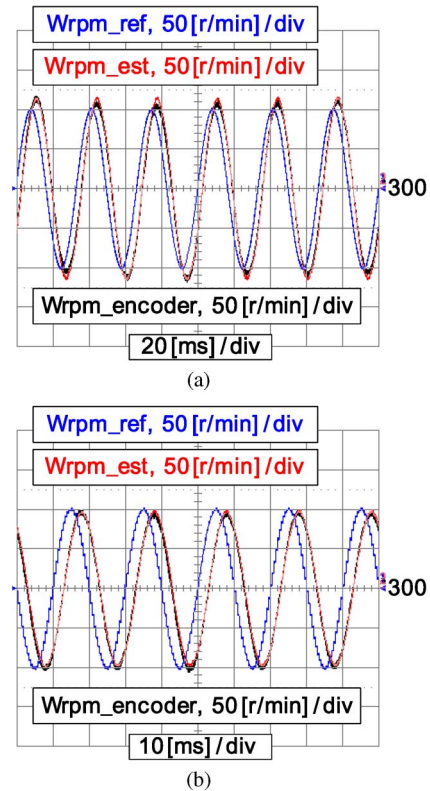


Fig. 20. Speed estimation performance of the position observer. (a) 30-Hz operation. (b) 50-Hz operation.

Fig. 20 shows the speed estimation performance. The experimental condition of Fig. 20 was the same as that of Fig. 17. In these figures, the speed reference (W_{rpm_ref}), the estimated speed (W_{rpm_est}), and the speed from the encoder ($W_{rpm_encoder}$) are displayed. “ $W_{rpm_encoder}$ ” is the calculated speed by the M/T method [20] with the encoder used for the monitoring purpose. Therefore, it can be considered as a real speed. The speed reference is the signal which has the most

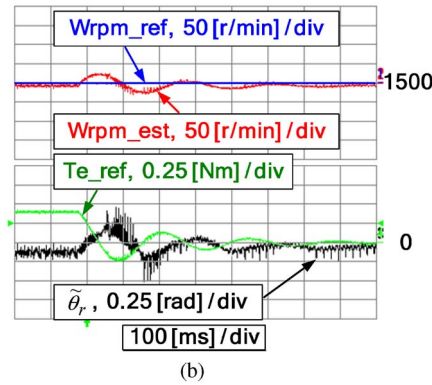
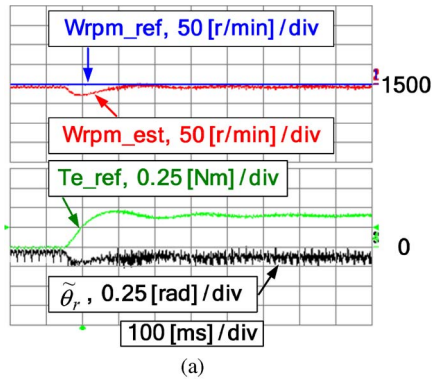


Fig. 21. Stiffness of the proposed sensorless algorithm with load variation. (a) From 0% to 80%. (b) From 80% to 0%.

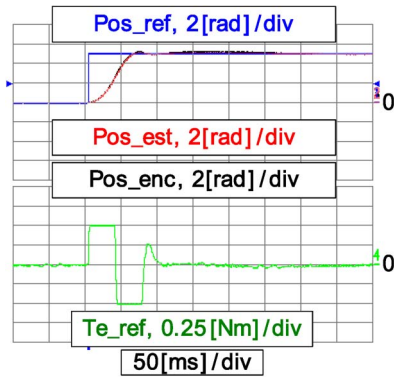


Fig. 22. Step response of the position controller.

leading phase. Moreover, the other two signals are almost the same as each other. As shown in these figures, the estimated speed was identical with the real speed. From these results, it can be concluded that the speed estimation by the position observer was performed quite well.

Fig. 21 shows the dynamic stiffness of the proposed sensorless control algorithm. On a constant speed operation of 1500 r/min, sudden load torque was applied by a load machine, dc generator. The load was varied from 0% to 80% and vice versa. Due to limitations of the load machine, a load over 80% could not be applied. As shown in Fig. 21, the position estimation error was maintained within ± 0.25 rad, even if the load torque varied rapidly.

Fig. 23 shows the sine wave response of the position controller. Signals in Fig. 23 are the same as those in Fig. 22. The magnitude of the position reference was 1 rad, and the

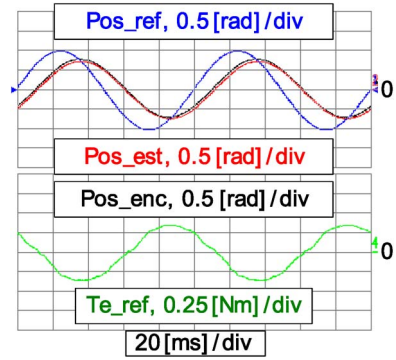


Fig. 23. Position regulation performance.

frequency was 10 Hz. As shown in the figure, the bandwidth of the position controller is around 10 Hz, which is the designed value.

Experiments on position control mode were also performed. The position controller consists of only P controller. Bandwidths of the speed controller and position controller were set as 50 and 10 Hz. Fig. 22 shows the step response of the position controller with the references of 0 to 5 rad. In the figure, the position reference (Pos_ref), estimated position (Pos_est), position from the encoder (Pos_enc), and torque reference (Te_ref) are displayed. “Pos_enc” can be considered as a real position. As shown in Fig. 22, Pos_est was identical with “Pos_enc,” and position was well regulated.

The same experiments were also performed with an 11-kW general-purpose IPMSM. The bandwidths of the speed controller and position controller can be extended up to 25 and 5 Hz by the proposed method, respectively. Due to the page limitation, the results were omitted in this paper.

V. CONCLUSION

This paper has proposed a new sensorless algorithm. It contains a voltage injection method, a signal processing method, and a position observer. Based on the square-wave-type high-frequency voltage injection, a new rotor position estimation method is proposed. The estimated position has a little noise but virtually no delay.

Using the proposed method, the poles of the position observer can be set at 50 Hz. The bandwidth of the speed controller and position controller can be set as 50 and 10 Hz, respectively. By increasing the injection frequency up to a half of the switching frequency, the fundamental frequency is definitely separated from the injection frequency. Moreover, the bandwidth of the current controller is increased up to 250 Hz. As a result, the stability, repeatability, bandwidth, and dynamic stiffness of the proposed sensorless control method have been enhanced conspicuously compared to that of a conventional method.

The feasibility and effectiveness of the proposed method have been verified through the experimental results and theoretical analysis. Moreover, it can be easily applied to any ac servo drive system driven by a PWM inverter and a digital controller if the motor has saliency in rotor impedance at the injected high frequency.

REFERENCES

- [1] M. Tursini, R. Petrella, and F. Prasiliti, "Sensorless control of an IPM synchronous motor for city-scooter application," in *Conf. Rec. IEEE IAS Annu. Meeting*, Oct. 2003, pp. 1472–1479.
- [2] R. Raute and N. Ertugrul, "Sensorless permanent magnet ac motor drive with near zero-speed operation for electric-assisted bicycle," in *Proc. EPE*, Dresden, Germany, Sep. 2005, pp. 5024–5033.
- [3] K. Ide, M. Takaki, S. Morimoto, Y. Kawazoe, A. Maemura, and M. Ohto, "Saliency-based sensorless drive of adequate designed IPM motor for robot vehicle application," in *Conf. Rec. PCC*, Apr. 2007, pp. 1126–1133.
- [4] S. Ogasawara and H. Akagi, "An approach to position sensorless drive for brushless dc motor," *IEEE Trans. Ind. Appl.*, vol. 27, no. 5, pp. 928–933, Sep./Oct. 1991.
- [5] K. D. Hurst, T. G. Habetler, G. Griva, and F. Profumo, "Zero-speed tachless IM torque control: Simply a matter of stator voltage integration," *IEEE Trans. Ind. Appl.*, vol. 34, no. 4, pp. 790–795, Jul./Aug. 1998.
- [6] A. B. Kulkarni and M. Ehsani, "A novel position sensor elimination technique for interior permanent-magnet synchronous drive," *IEEE Trans. Ind. Appl.*, vol. 28, no. 1, pp. 144–150, Jan./Feb. 1992.
- [7] R. B. Sepe and J. H. Lang, "Real-time observer-based (adaptive) control of a permanent-magnet synchronous motor without mechanical sensors," *IEEE Trans. Ind. Appl.*, vol. 28, no. 6, pp. 1345–1352, Nov./Dec. 1992.
- [8] M. Schroedl, "Sensorless control of ac machines at low speed and standstill based on the 'INFORM' method," in *Conf. Rec. 31st IEEE IAS Annu. Meeting*, Oct. 6–10, 1996, vol. 1, pp. 270–277.
- [9] S. Ogasawara and H. Akagi, "Implementation and position control performance of a position-sensorless IPM motor drive system based on magnetic saliency," *IEEE Trans. Ind. Appl.*, vol. 34, no. 4, pp. 806–812, Jul./Aug. 1998.
- [10] P. L. Jansen and R. D. Lorenz, "Transducerless position and velocity estimation in induction and salient ac machines," *IEEE Trans. Ind. Appl.*, vol. 31, no. 2, pp. 240–247, Mar./Apr. 1995.
- [11] Y. Jeong, R. D. Lorenz, T. M. Jahns, and S. K. Sul, "Initial rotor position estimation of an interior permanent-magnet synchronous machine using carrier-frequency injection methods," *IEEE Trans. Ind. Appl.*, vol. 41, no. 1, pp. 38–45, Jan./Feb. 2005.
- [12] J. I. Ha and S. K. Sul, "Sensorless field-orientation control of an induction machine by high-frequency signal injection," *IEEE Trans. Ind. Appl.*, vol. 35, no. 1, pp. 45–51, Jan./Feb. 1999.
- [13] J. I. Ha, K. Ide, T. Sawa, and S. K. Sul, "Sensorless position control and initial position estimation of an interior permanent magnet motor," in *Conf. Rec. IEEE IAS Annu. Meeting*, Sep. 2001, vol. 4, pp. 2607–2613.
- [14] M. J. Corley and R. D. Lorenz, "Rotor position and velocity estimation for a permanent magnet synchronous machine at standstill and high speeds," in *Conf. Rec. IEEE IAS Annu. Meeting*, 1996, vol. 1, pp. 36–41.
- [15] J. H. Jang, S. K. Sul, J. I. Ha, K. Ide, and M. Sawamura, "Sensorless drive of surface-mounted permanent-magnet motor by high-frequency signal injection based on magnetic saliency," *IEEE Trans. Ind. Appl.*, vol. 39, no. 4, pp. 1031–1039, Jul./Aug. 2003.
- [16] K. Ide, J. K. Ha, and M. Sawamura, "A hybrid speed estimation of flux observer for induction motor drives," *IEEE Trans. Ind. Electron.*, vol. 53, no. 1, pp. 130–137, Feb. 2006.
- [17] A. Consoli, G. Scarcella, and A. Testa, "A new zero-frequency flux position detection approach for direct-field-oriented-control drives," *IEEE Trans. Ind. Appl.*, vol. 36, no. 3, pp. 797–804, May/Jun. 2000.
- [18] J. Holtz, "Sensorless control of induction motor drives," *Proc. IEEE*, vol. 90, no. 8, pp. 1359–1394, Aug. 2002.
- [19] J. S. Kim, J. W. Choi, and S. K. Sul, "Analysis and compensation of voltage distortion by zero current clamping in voltage-fed PWM inverter," in *Conf. Rec. IPEC*, Yokohama, Japan, 1995, pp. 265–270.
- [20] T. Ohmae, T. Matsuda, K. Kamiyama, and M. Tachikawa, "A microprocessor-controlled high-accuracy wide-range speed regulator for motor drives," *IEEE Trans. Ind. Electron.*, vol. IE-29, no. 3, pp. 207–211, Aug. 1982.



Young-Doo Yoon (S'06–M'10) was born in Seoul, Korea, in 1978. He received the B.S., M.S., and Ph.D. degrees in electrical engineering from Seoul National University, Seoul, Korea, in 2002, 2005, and 2010, respectively.

Since 2010, he has been a Senior Engineer with Samsung Electronics Company, Suwon, Korea. His current research interests are power electronics control of electric machines, electric vehicle drives, and matrix converter drives.



Seung-Ki Sul (S'78–M'80–SM'98–F'00) was born in Korea in 1958. He received the B.S., M.S., and Ph.D. degrees in electrical engineering from Seoul National University, Seoul, Korea, in 1980, 1983, and 1986, respectively.

From 1986 to 1988, he was an Associate Researcher in the Department of Electrical and Computer Engineering, University of Wisconsin, Madison. From 1988 to 1990, he was a Principal Research Engineer with Gold-Star Industrial Systems Company. Since 1991, he has been a member of the

faculty of the School of Electrical Engineering, Seoul National University, where he is currently a Professor. His current research interests are power electronic control of electric machines, electric/hybrid vehicle drives, and power-converter circuits.



Shinya Morimoto received the B.S. degree in control engineering from Kyushu Institute of Technology, Kitakyushu, Japan, in 1990.

In 1990, he joined Yaskawa Electric Corporation, Kitakyushu, where he is currently Manager of the Power Electronics Team at the Corporate R&D Center. He is interested in the design and development of motor-drive control and power conversion.

Mr. Morimoto is a member of the Society of Instrument and Control Engineers of Japan.



Kozo Ide (S'92–M'96) received the B.S., M.S., and Ph.D. degrees in electrical engineering from Kyushu Institute of Technology, Kitakyushu, Japan, in 1991, 1993, and 1996, respectively.

From 1991 to 1992, he was a Visiting Researcher at L'Aquila University, L'Aquila, Italy, supported by the Italian government. In 1996, he joined Yaskawa Electric Corporation, Kitakyushu, where he is currently Manager of R&D of motor drive control. From 2002 to July 2003, he was a Visiting Researcher at Siemens AG, Germany. His current research interests

are control technology for ac machines and energy conversion systems.

Dr. Ide is a member of the Institute of Electrical Engineers of Japan.